

**Effect of Support Redox Character on Catalytic
Performance in the Gas Phase Hydrogenation of
Benzaldehyde and Nitrobenzene over Supported Gold**

**Maoshuai Li, Xiaodong Wang, Fernando Cárdenas-Lizana*
and Mark A. Keane**

**Chemical Engineering, School of Engineering and Physical Sciences,
Heriot-Watt University, Edinburgh EH14 4AS, Scotland**

*corresponding author

Tel: +44(0)131 451 4115, e-mail: f.cardenaslizana @hw.ac.uk

ABSTRACT

A range of oxides (γ -Al₂O₃, TiO₂, ZrO₂, CeO₂, α -Fe₂O₃ and Fe₃O₄) with different redox properties were used to support nano-scale (mean = 2-8 nm) Au and employed in the gas phase hydrogenation of benzaldehyde and nitrobenzene. The catalysts were subjected to TPR, H₂/O₂ titration, H₂ TPD, XRD, TEM/STEM and XPS analysis. The supported Au phase promoted partial reduction of the reducible supports through the action of spillover hydrogen (based on TPD), which generated surface oxygen vacancies (demonstrated by O₂ titration) that inhibit Au particle sintering during catalyst activation. Electron transfer to generate charged Au species (determined by XPS) correlates with support ionisation potential. Higher nitrobenzene hydrogenation (to aniline) *TOFs* were recorded relative to benzaldehyde where rate increased with decreasing Au size (from 8 to 4 nm) with measurably lower *TOF* over Au <3 nm. Strong binding of -CH=O and -NO₂ functions to oxygen vacancies resulted in lower hydrogenation rates. Higher temperatures (>413 K) promoted benzaldehyde hydrogenolysis to toluene and benzene. The formation of Au^{δ-} on non-reducible Al₂O₃ favoured selective reduction of -CH=O with full selectivity to benzyl alcohol at 413 K.

Keywords: Selective hydrogenation; benzaldehyde; nitrobenzene; reducible supports; oxygen vacancies; Au particle size effect.

1. Introduction

The selective hydrogenation of benzaldehyde to benzyl alcohol and nitrobenzene to aniline are important in the production of herbicides, dyes, pigments and fine chemicals [1,2]. Conventional batch synthesis delivers low product yields, is energy inefficient and generates significant waste where exclusive reduction of the carbonyl and nitro group is challenging [3]. Continuous gas phase reaction presents a number of advantages including ease of product/catalyst separation and reduced downtime [4]. Supported Au at the nano-scale (<10 nm) exhibits unique selectivity in the hydrogenation of multi-functional reactants although activity is lower compared with conventional transition metals (Pt, Ru, Pd and Ni) [5] due to the limited capacity of Au to chemisorb/dissociate H₂ [6]. Studies to date on the catalytic hydrogenation of carbonyl (acrolein, benzalacetone, cinnamaldehyde and crotonaldehyde) [7,8] and nitro (chloronitrobenzene, nitrostyrene and nitrobenzaldehyde) [9,10] compounds have shown a dependence on the electronic and geometric properties of the Au phase that are influenced by the support. Smaller Au particles are formed on reducible oxides (*e.g.* TiO₂ and CeO₂) relative to non-reducible ZrO₂ and SiO₂ [11,12]. Higher turnover frequencies (*TOF*) with decreasing Au size (2-9 nm) has been reported in the hydrogenation of crotonaldehyde [11,13] and nitrobenzene [14] for Au supported on TiO₂, Al₂O₃ and SiO₂. Okumura *et al.* [11] observed higher alcohol selectivity (from crotonaldehyde) over Au/TiO₂ than Au/Al₂O₃ and Au/SiO₂. Milone and co-workers [15] proposed that reducible iron oxides promote the formation of electron-rich Au through metal-support electron transfer that favours –CH=O reduction. Rojas *et al.* [16] concluded that negatively charged Au (on SiO₂) binds the electrophilic carbon in –CH=O facilitating hydrogenation of cinnamaldehyde and benzalacetone.

In nitro group reduction, the high selectivity exhibited by Au/TiO₂ has been attributed to metal-support synergy that promotes –NO₂ activation [17]. Shimizu *et al.* [18] considered the

role of Al₂O₃ acidity/basicity in tandem with coordinatively unsaturated Au to dissociate H₂ to H⁺/H⁻ at the metal/support interface and selectively reduce –NO₂ in the presence of other reactive functionalities. In the hydrogenation of *p*-chloronitrobenzene unwanted hydrodechlorination was reported for Au/Ce_{0.62}Zr_{0.38}O₂ and ascribed to C–Cl scission at oxygen vacancy sites [19]. Selective hydrogenation has been well established for Au catalysts but the contribution of the support in modifying Au structure, reactant activation and overall surface reaction mechanism is far from resolved. In this study we compare the catalytic action of Au nanoparticles on oxides (γ-Al₂O₃, ZrO₂, TiO₂, CeO₂, α-Fe₂O₃ and Fe₃O₄) with distinct redox character in the hydrogenation of –CH=O (benzaldehyde) and –NO₂ (nitrobenzene) and correlate performance with catalyst structure. We propose surface reaction mechanisms to account for the role of support reducibility in governing –CH=O and –NO₂ activation and product selectivity.

2. Experimental

2.1. Catalyst preparation and activation

The supports employed in this study were obtained from commercial sources (γ-Al₂O₃ (Puralox, Condea Vista), TiO₂ (P25, Degussa) and CeO₂ (Grace Davison)) or synthesised (α-Fe₂O₃, Fe₃O₄ and ZrO₂) as described elsewhere [12,20]. Supported Au catalysts were prepared by deposition-precipitation using urea (Riedel-de Haën, 99%) as basification agent. An aqueous solution of urea (100-fold excess) and HAuCl₄ (3-7 × 10⁻³ M, 400 cm³, Sigma Aldrich, 99%) was added to the support (10-30 g). The suspension was stirred and heated (2 K min⁻¹) to 353 K where the pH progressively increased (to 6.5-8.0) as a result of urea decomposition:



The solid obtained was separated by filtration, washed with distilled water until Cl free (from AgNO₃ test) and dried (2 K min⁻¹) in 45 cm³ min⁻¹ He at 373 K for 5 h. The catalyst

precursors were sieved (ATM fine test sieves) to mean particle diameter = 75 μm and activated at 2 K min^{-1} to 423-673 K in 60 $\text{cm}^3 \text{min}^{-1}$ H_2 . The catalysts were cooled to ambient temperature and passivated in 1% v/v O_2/He for off-line characterisation.

2.2. Catalyst characterisation

Gold content was measured by atomic absorption spectroscopy (Shimadzu AA-6650 spectrometer with an air-acetylene flame) from the diluted extract in aqua regia (25% v/v HNO_3/HCl). The pH associated with the point of zero charge (pH_{pzc}) of the support was determined using the potentiometric mass titration technique described in detail elsewhere [21]. Temperature programmed reduction (TPR), H_2 chemisorption/temperature programmed desorption (TPD), O_2 chemisorption and specific surface area (SSA) measurements were conducted on the CHEM-BET 3000 (Quantachrome) unit equipped with a thermal conductivity detector (TCD) for continuous monitoring of gas composition and the TPR WinTM software for data acquisition/manipulation. Samples were loaded into a U-shaped Pyrex quartz cell (3.76 mm i.d.) and heated in 17 $\text{cm}^3 \text{min}^{-1}$ (Brooks mass flow controlled) 5% v/v H_2/N_2 at 2 K min^{-1} to 423-673 K for supported Au catalysts and to 1073-1273 K for the supports where the effluent gas passed through a liquid N_2 trap. The activated samples were swept with 65 $\text{cm}^3 \text{min}^{-1}$ N_2 for 1.5 h, cooled to reaction temperature (413 K) and subjected to a H_2 (BOC, >99.98%) pulse (10 μl) titration procedure. Samples were cooled to ambient temperature, thoroughly flushed in N_2 (65 $\text{cm}^3 \text{min}^{-1}$) to remove weakly bound H_2 and subjected to TPD (at 50 K min^{-1}) to 873-1173 K with a final isothermal hold until the signal returned to baseline. Oxygen (BOC, 99.9%) pulse (50 μl) titration at 413 K post-TPR was employed to determine the extent of support reduction where any contribution from Au to total O_2 adsorption is negligible [22]. SSA (reproducible to $\pm 8\%$) was recorded in 30% v/v N_2/He with undiluted N_2 (BOC, 99.9%) as internal standard. At least three cycles of N_2 adsorption-desorption were employed using the standard single point BET method. Pore

volume was measured using the Micromeritics Gemini VII 2390p system. Prior to analysis, samples were outgassed at 423 K for 1 h in N₂. Total pore volume was obtained at a relative N₂ pressure (P/P_0) = 0.95. X-ray diffractograms (XRD) were recorded on a Bruker/Siemens D500 incident X-ray diffractometer using Cu K α radiation. Samples were scanned at 0.02° step⁻¹ over the range $20^\circ \leq 2\theta \leq 80^\circ$ and the diffractograms identified against the JCPDS-ICDD reference standards, *i.e.* Au (04-0784), γ -Al₂O₃ (10-0425), anatase-TiO₂ (A-TiO₂, 21-1272), rutile-TiO₂ (R-TiO₂, 21-1276), monoclinic-ZrO₂ (M-ZrO₂, 37-1784), tetragonal-ZrO₂ (T-ZrO₂, 50-1089), CeO₂ (43-1002), α -Fe₂O₃ (hematite, 33-0664) and Fe₃O₄ (magnetite, 19-0629). X-ray photoelectron spectroscopic (XPS) analysis was performed on a VG ESCA spectrometer equipped with monochromatised Al K α radiation (1486 eV). The sample was adhered to conducting carbon tape, mounted in the sample holder and subjected to ultra-high vacuum conditions (<10⁻⁸ Torr). Full range surveys (Au 4f_{5/2} and 4f_{7/2} spectra) were collected where the binding energies (BE) were calibrated with respect to the C 1s peak (284.5 eV). The Au 4f spectra were fitted with abstraction of the Shirley background using the Gaussian-Lorentzian function in XPSPEAK 41. Gold particle morphology (size and shape) was examined by transmission (TEM, JEOL JEM 2011) and scanning transmission (STEM, JEOL 2200FS field emission gun-equipped unit) electron microscopy, employing Gatan Digital Micrograph 1.82 for data acquisition/manipulation. Samples for analysis were dispersed in acetone and deposited on a holey carbon/Cu grid (300 Mesh). The surface area weighted mean Au size (d) was based on a count of at least 300 particles according to

$$d = \frac{\sum_i n_i d_i^3}{\sum_i n_i d_i^2} \quad (2)$$

where n_i is the number of particles of diameter d_i .

2.3. Catalytic procedure

Catalyst testing was carried out at atmospheric pressure, *in situ* after activation, in a continuous flow fixed bed tubular reactor (i.d. = 15 mm) at 413-573 K under conditions of negligible heat/mass transport limitations. A layer of borosilicate glass beads served as preheating zone, ensuring the organic reactant was vaporised and reached reaction temperature before contacting the catalyst (10-40 mg). Isothermal conditions (± 1 K) were maintained by diluting the catalyst bed with ground glass (75 μm). Reaction temperature was continuously monitored by a thermocouple inserted in a thermowell within the catalyst bed. Reactants (benzaldehyde (Fluka, $\geq 98\%$), nitrobenzene (Riedel-de Haën, $\geq 99\%$) or benzyl alcohol (Riedel-de Haën, $\geq 99\%$)) were delivered as an ethanolic (Sigma Aldrich, $\geq 99\%$) solution to the reactor *via* a glass/teflon air-tight syringe and teflon line using a microprocessor controlled infusion pump (Model 100 kd Scientific) at a fixed calibrated flow rate. Reactions were conducted in a co-current flow of reactant with H_2 (BOC, $>99.98\%$, 60 $\text{cm}^3 \text{min}^{-1}$) at $GHSV = 2 \times 10^4 \text{ h}^{-1}$. The molar Au to inlet organic molar feed rate (n/F) spanned the range $1.2 \times 10^{-3} - 3.7 \times 10^{-3} \text{ h}$. In blank tests, passage of each reactant in a stream of H_2 through the empty reactor or over the support did not result in any detectable conversion. The reactor effluent was collected in a liquid nitrogen trap for subsequent analysis using a Perkin-Elmer Auto System XL gas chromatograph equipped with a programmed split/splitless injector and a flame ionization detector (FID), employing a DB-1 (50 m \times 0.33 mm i.d., 0.20 μm film thickness) capillary column (J&W Scientific). Data acquisition and manipulation were performed using the TurboChrom Workstation Version 6.3.2 (for Windows) chromatography data system. Reactant conversion (X) is defined by

$$X (\%) = \frac{[\text{reactant}]_{\text{in}} - [\text{reactant}]_{\text{out}}}{[\text{reactant}]_{\text{in}}} \times 100 \quad (3)$$

and selectivity (S) to product (j) is given by

$$S_j(\%) = \frac{[product]_{j, out}}{[reactant]_{in} - [reactant]_{out}} \times 100 \quad (4)$$

where subscripts “in” and “out” refer to inlet and outlet gas streams. Catalytic activity is also quantified in terms of initial conversion obtained from time on-stream measurements and turnover frequency (*TOF*, rate per active site) calculated using Au dispersion (*D*) obtained from STEM analysis [23] according to:

$$TOF \text{ (h}^{-1}\text{)} = \frac{R}{D} \quad (5)$$

where *R* represents reactant consumption rate ($\text{mol}_{\text{reactant}} \text{ mol}_{\text{metal}}^{-1} \text{ h}^{-1}$). Repeated reactions with different samples from the same batch of catalyst delivered raw data reproducibility and mass balances within ± 5 %.

3. Results and discussion

3.1. Catalyst characterisation

3.1.1. Structural characteristics and temperature programmed reduction (TPR)

Catalyst physico-chemical characteristics are presented in **Table 1**. SSA range from 11 $\text{m}^2 \text{ g}^{-1}$ (Au/Fe₃O₄) to 166 $\text{m}^2 \text{ g}^{-1}$ (Au/ γ -Al₂O₃) with a corresponding increase in pore volume (0.02-0.36 $\text{cm}^3 \text{ g}^{-1}$). Values obtained for each catalyst are in good agreement with those reported in the literature [24-27]. The TPR profiles of the supported Au catalyst precursors and corresponding supports are presented in **Fig. 1**. TPR of Au/ γ -Al₂O₃ (**AI**) and Au/ZrO₂ (**CI**) generated positive signals with associated temperature maxima (T_{max}) at 451 and 476 K, respectively where H₂ consumption matched the requirement for Au³⁺ reduction to Au⁰ (**Table 1**). The profiles generated for the γ -Al₂O₃ (**AII**) and ZrO₂ (**CII**) supports were featureless with no evidence of H₂ uptake or release, as noted elsewhere [25]. Activation of Au/TiO₂ (**BI**) and Au/CeO₂ (**DI**) presented H₂ consumption peaks at lower temperatures ($T_{\text{max}} = 364$ and 420 K) suggesting weaker metal-support interactions. This is consistent with the work of Delannoy *et al.* [28] who examined the effect of support redox character on Au

reducibility and reported more facile reduction on TiO₂ and CeO₂ relative to Al₂O₃. Hydrogen consumed during TPR of Au/TiO₂ exceeded that required for Au³⁺ → Au⁰ (**Table 1**) and can be attributed to a combined Au reduction with Ti⁴⁺ conversion to Ti³⁺ at the metal/support interface [29]. The bare TiO₂ support did not exhibit a detectable TPR response (**BII**). In contrast, thermal treatment of CeO₂ generated two broad signals at 742 K and 1148 K (**DII**) that can be ascribed to surface (523-848 K [30]) and bulk (>1073 K [30]) reduction. Hydrogen consumed during the activation of Au/CeO₂ exceeded Au precursor reduction (**Table 1**) but was significantly lower than the amount needed for full reduction of the CeO₂ carrier (3300 μmol g⁻¹). This suggests partial support reduction where the incorporation of Au on CeO₂ lowered the requisite temperature [31]. TPR of Au/α-Fe₂O₃ (**EI**) resulted in excess H₂ consumption at $T_{\max} = 389$ K whereas TPR of α-Fe₂O₃ (**EII**) generated a signal at 709 K with a broader consumption at $T > 800$ K suggesting a two-stage reduction of hematite, *i.e.* α-Fe₂O₃ → Fe₃O₄ → FeO. The TPR response for Au/Fe₃O₄ (**FI**) also reveals a down shift in T_{\max} relative to the support (**FII**). The excess H₂ consumed (**Table 1**) fell below that for conversion of Fe₃O₄ to FeO (4250 μmol g⁻¹) again indicative of partial support reduction. Our results demonstrate a more facile reduction of ceria and iron oxide supports due to the presence of Au. Jacobs *et al.* [32] have established partial CeO₂ reduction by spillover hydrogen following dissociative adsorption on supported Au. Furthermore, Scirè and co-workers [33] proposed that Au can weaken the Fe-O bond in iron oxide substrates resulting in greater lattice oxygen mobility and enhanced reducibility.

3.1.2. Hydrogen temperature programmed desorption (TPD) and O₂ chemisorption

Application of TPD to measure surface hydrogen release can allow differentiation between chemisorbed and spillover species which both serve as reactive hydrogen in hydrogenation [34]. The TPD profiles generated for all the catalysts are shown in **Fig. 2**. The literature suggests a lower temperature requirement for H₂ desorption from metal sites (<473

K) compared with release of spillover from the support (>503 K) [35]. A predominant H₂ desorption at $T_{max} \geq 575$ K was observed in this work suggesting that the main contribution is due to spillover. Hydrogen spillover is influenced by the concentration of initiating and acceptor sites, catalyst activation and metal nanoparticle size (*i.e.* degree of contact between participating phases and metal-support interaction(s)) [35]. As a general observation, H₂ release from Au supported on non-reducible (Al₂O₃, ZrO₂) supports (28-51 mmol g_{Au}⁻¹) was significantly greater than that recorded for Au on reducible carriers (≤ 9 mmol g_{Au}⁻¹). There is compelling evidence in the literature for hydrogen spillover onto Al₂O₃ [34,35] and ZrO₂ [36,37] from supported metals (Pd, Ni, Cu and Ru). The greater H₂ desorption from Au/ γ -Al₂O₃ relative to Au/ZrO₂ can be attributed (at least in part) to the higher SSA of Al₂O₃ which can accommodate more spillover. Consumption of spillover hydrogen in the partial reduction of (reducible) titania, ceria and iron oxide can account for the observed lower levels of H₂ TPD [34]. We employed O₂ chemisorption post-TPR as a measure of support reduction [22]. Gold on CeO₂, α -Fe₂O₃ and Fe₃O₄ exhibited greater O₂ uptake (**Table 1**) than that measured for Au/TiO₂, Au/ γ -Al₂O₃ and Au/ZrO₂. The difference in O₂ adsorption can be correlated with support redox character [38], where the former group of oxides are characterised by higher redox potentials (E_{redox}) (**Table 1**). Increasing O₂ chemisorption coincided with greater excess H₂ consumption during TPR due to support reduction with the formation of oxygen vacancies. Oxygen deficient sites can be generated by loss of lattice oxygen from reducible metal oxides during thermal treatment in H₂ or CO [39]. Boccuzzi *et al.* [40,41] demonstrated by FTIR spectroscopy the formation of oxygen vacancies following reduction in H₂ of Fe₂O₃, TiO₂ and CeO₂ to 523 K. Moreover, formation of Ce³⁺ defects/surface vacancies in Au/CeO₂-Fe₂O₃ has been linked to the action of spillover hydrogen [42].

3.1.3. X-ray diffraction (XRD) and electron microscopy analysis

Structural analysis by XRD generated the diffractograms presented in **Fig. 3**. There was no clearly discernible peak for Au (at $2\theta = 38.1^\circ$) which may be due to masking by stronger signals due to the support or the formation of Au particles at the nano-scale and below detection limit (<5 nm) [43]. The XRD pattern of Au/ γ -Al₂O₃ is characterised by peaks at $2\theta = 37.6^\circ, 39.5^\circ, 45.9^\circ$ and 67.0° due to cubic γ -Al₂O₃. XRD analysis of Au/TiO₂ revealed a mixture of tetragonal anatase ($2\theta = 25.3^\circ, 37.8^\circ, 48.1^\circ$ and 62.8°) and tetragonal rutile ($2\theta = 27.4^\circ, 36.1^\circ, 41.2^\circ, 54.3^\circ, 56.6^\circ, 69.0^\circ$ and 69.8°) phases with an anatase:rutile ratio (5:1) that matches the reported Degussa P25 composition [44]. Au/ZrO₂ showed mixed monoclinic ($2\theta = 28.2^\circ, 31.5^\circ, 34.2^\circ, 34.4^\circ, 35.3^\circ, 40.8^\circ, 49.3^\circ, 50.2^\circ, 50.6^\circ$ and 55.6°) and tetragonal ($2\theta = 30.3^\circ, 35.3^\circ, 50.4^\circ, 50.7^\circ, 59.6^\circ$ and 60.2°) phases with monoclinic/tetragonal ~ 2 . Zirconia phase composition is sensitive to synthesis route and calcination temperature with ratios in the range 1.2-3.2 reported for comparable ZrO₂ preparation and pre-treatment [25]. The XRD patterns of Au on CeO₂, α -Fe₂O₃ and Fe₃O₄ (**Fig. 3(D-F)**) match those of the supports and we can discount bulk support reduction, *i.e.* CeO₂ \rightarrow Ce₂O₃, Fe₂O₃ \rightarrow Fe₃O₄ and/or Fe₃O₄ \rightarrow FeO.

Gold particle morphology was evaluated by TEM/STEM and the representative images in **Fig. 4** reveal quasi-spherical particles at the nano-scale. Surface area weighted mean Au size was obtained from the size distribution histograms and are recorded in **Table 1**. Gold on γ -Al₂O₃ (**A**) exhibited metal particles in the 1-8 nm range with a mean of 4.3 nm. Appreciably larger Au particles (2-12 nm, mean = 7.0 nm) are observed on ZrO₂ (**C**), consistent with the report of Mohr *et al.* [45] for Au/ZrO₂ preparation by deposition-precipitation. Reducible CeO₂ (**D**) and α -Fe₂O₃ (**E**) supports show narrower Au size distribution (1-5 nm) and smaller mean values (2.0-2.6 nm) than Au/TiO₂ (**B**), 1-9 nm, mean = 4.5 nm). Support oxygen vacancies stabilise transition metal nanoparticles and inhibit

sintering [46], which may result in the formation of smaller Au particles on α -Fe₂O₃ and CeO₂ that bear a greater number of vacancies than Au/TiO₂ (**Table 1**). It should be noted that a wider Au size range and mean (\approx 7.6 nm) characterised Au/Fe₃O₄. Support charge density, reflected in the pH point of zero charge (pH_{pzc}), determines precursor-support interaction in synthesis by deposition-precipitation and can govern ultimate Au size post-TPR. Where solution pH < pH_{pzc}, the support bears a positive charge favouring interaction with anionic Au species. Conversely, where solution pH > pH_{pzc} the Au precursor and support experience repulsive effects due to the negative surface charge resulting in weaker Au-support interaction leading to Au agglomeration during activation [47]. Solution pH controls AuCl₄⁻ hydrolysis rate *via* substitution of Cl⁻ by OH⁻ where Au(OH)₄⁻ predominates at the final pH (6.5-8.0, see experimental section **2.1**) [48]. Support pH_{pzc} are given in **Table 1** where the lower value for Fe₃O₄ (5.8) does not favour interaction with (anionic) Au precursor species and can account for larger Au size.

3.1.4. X-ray photoelectron spectroscopy (XPS) analysis

XPS measurements were conducted to probe support effects in modifying Au electronic character. XPS profiles over the Au 4*f* binding energy (BE) region are given in **Fig. 5**. The Au 4*f*_{7/2} BE for Au/ γ -Al₂O₃ (83.3 eV) and Au/TiO₂ (83.5 eV) are close to values reported in the literature (Au/Al₂O₃ (83.1 eV) [49] and Au/TiO₂ (83.3 eV) [50]) and fall below the reference metallic Au (83.7-84.0 eV) [51], indicative of electron donation from the support [52]. Gold on CeO₂ (**Table 1**) exhibits an Au 4*f*_{7/2} BE consistent with that published for Au/CeO₂ (84.5 eV) [53] but lower than Au⁺ (85.8-86.0 eV) [51]. A partial positive charge (Au ^{δ +}) has been proposed for Au/CeO₂ resulting from electron transfer from Au [54]. The data presented in **Fig. 6** show a dependence of Au 4*f*_{7/2} BE on support redox potential where electron transfer from Au is facilitated by carriers with higher potential. Gold electronic structure is also dependent on Au cluster size where any shift in BE is more pronounced with decreasing

coordination number [55]. The formation of smaller particles on Au/CeO₂ can also contribute to an upshift of BE.

3.2. Catalyst activity/selectivity

Benzyl alcohol was the sole product detected in the hydrogenation of benzaldehyde at 413 K. In contrast, gas phase (383-413 K) benzaldehyde conversion over (SiO₂, Al₂O₃, TiO₂, CeO₂ and ZrO₂) supported Cu and Ni resulted in –CH=O hydrogenolysis (to toluene) and/or C–C scission (to benzene) [56,57]. The relationship between benzaldehyde turnover frequency (*TOF* at 413 K) and Au particle size (*d*) is shown in **Fig. 7(I)**. An increase in *TOF* is evident with decreasing Au particle size over the 8-4 nm range which can be linked to greater H₂ uptake under reaction conditions (**Table 1**). The highest specific rate was recorded for Au/γ-Al₂O₃ with no detectable activity for catalysts bearing the smallest Au sizes (Au/α-Fe₂O₃ and Au/CeO₂). It has been established that Au exhibits metal to insulator transition for particles ≤3 nm [58] and decreasing hydrogenation activity for smaller Au particles (5→1 nm) has been ascribed to a critical loss of metallic character [59]. Although there is insufficient published data to arrive at any reliable trends regarding Au size effects in –CH=O hydrogenation, we can note the reported decrease in acrolein *TOF* over Au/ZrO₂ for Au particles >4 nm [45] and increase with increasing Au size (1-5 nm) over Au/ZrO₂ and Au/TiO₂ [59]. In contrast to the benzaldehyde reaction, each catalyst was active in nitrobenzene hydrogenation (**Fig. 7(II)**) with a *TOF* maximum for Au/γ-Al₂O₃. The greater reactivity of the nitro-reactant agrees with results (for Pt/Al₂O₃) reported by Arai *et al.* [60] where a six-fold higher rate was recorded for nitrobenzene relative to benzaldehyde hydrogenation. This was linked to reaction thermodynamics where nitrobenzene to aniline ($\Delta G_{413\text{ K}} = -436 \pm 1 \text{ kJ mol}^{-1}$) is more favourable than benzaldehyde hydrogenation to benzyl alcohol ($\Delta G_{413\text{ K}} = -24 \pm 2 \text{ kJ mol}^{-1}$).

With respect to support reducibility, *TOF* was higher at lower redox potential as shown in **Fig. 8**. Au/ZrO₂ deviates somewhat from the general trend, which we tentatively attribute to the occurrence of larger Au particles (**Fig. 4(C)**) that show low activity in hydrogenation. Lower *TOF* at higher redox potential suggests that oxygen vacancies on reducible supports do not favour –CH=O or –NO₂ activation for reaction. It is known that these vacancies can strongly bind adsorbed oxygenated species [61]. Gold on non-reducible γ -Al₂O₃ with the formation of Au^{δ-} (from XPS analysis) delivered the highest *TOF*. This agrees with published studies [16,62] which have shown that –CH=O activation and alcohol formation is facilitated on negatively charged Au *via* interaction with the electrophilic carbon. Given the negligible benzaldehyde hydrogenation activity over catalysts with smaller (<4 nm) and larger (>7 nm) Au particles at 413 K, we evaluated the effect of reaction temperature on rate and selectivity for Au/CeO₂ and Au/Fe₃O₄ which can be compared with Au/ γ -Al₂O₃ in **Table 2**. In each case an increase in *TOF* was observed at higher temperature. A switch was observed from exclusive –CH=O hydrogenation (to benzyl alcohol) at 413 K to hydrogenolysis (to toluene) at 473 K with a predominant aryl-carbonyl hydrogenolytic scission (to benzene) at 573 K over Au/ γ -Al₂O₃. A higher temperature (to 498 K) has been shown to promote benzaldehyde conversion to toluene and benzene over Cu/Al₂O₃ [56] and Ni/SiO₂ [63]. Benzaldehyde hydrogenation to benzyl alcohol was not observed over Au/Fe₃O₄ and Au/CeO₂ at any reaction temperature (**Table 2**). Increased temperature generated toluene as principal product with higher selectivity to benzene at 573 K (**Table 2**). Gold on redox supports exhibited a dominant hydrogenolytic character. Reaction of benzyl alcohol as feedstock (at 573 K) over Au/Fe₃O₄ generated toluene as principal product and benzaldehyde (with no detectable benzene) at a similar *TOF* to that recorded for the benzaldehyde reaction (**Table 3**). This points to production of toluene from benzaldehyde *via* consecutive conversion of benzyl alcohol whereas benzene is generated from aldehyde hydrogenolysis. Benzaldehyde was the

principal product in reaction over Au/CeO₂, which can be attributed to oxidative dehydrogenation [64]. This step involves the catalytic action of surface or lattice oxygens associated with the support and the high aldehyde selectivity exhibited by Au/CeO₂ (**Table 3**) must be due to greater oxygen mobility relative to Fe₃O₄ as inferred from O₂ chemisorption (**Table 1**).

Surface oxygen vacancies have been proposed as active sites in a range of applications from automobile exhaust treatment [65], water-gas shift [66] to steam reforming of oxygenates [67]. There is ample evidence that these vacancies can participate in a Mars and van Krevelen (MvK) mechanism with catalyst surface reduction (oxygen depletion) and re-oxidation (oxygen generation) [68]. We propose the involvement of oxygen vacancies in MvK catalytic hydrogenation, as illustrated in **Fig. 9**. The vacancies, created through H₂ chemisorbed on Au that spills onto the support (step A, **Fig. 9(I)**) with H₂O release, act as strong anchoring sites for the carbonyl group (steps B and C) [69], inhibiting reactivity. The stabilised carbonyl function can be activated at elevated temperature (473 K) with benzyl alcohol formation and subsequent hydrogenolysis (step D) or direct hydrogen scission of the –CH=O bond (step E) to benzene. Higher temperature facilitates hydrogen cleavage to give benzene (step F). In contrast, adsorption on non-reducible surfaces (*e.g.* Al₂O₃) *via* the carbonyl function (step A, **Fig. 10**) results in hydrogenation to the alcohol at low reaction temperature (413 K). DFT calculations have shown that a perpendicular adsorption mode is the most stable configuration with –CH=O bonded to the metal oxide surface *via* the oxygen lone electron pair that acts as a Lewis base [70]. FTIR analysis has demonstrated that surface Lewis acid sites on Al₂O₃ promote –CH=O activation in the hydrogenation of nitrobenzaldehyde [71]. Activation and scission of –CH₂–OH (steps B and C, **Fig. 10**), –CH=O (step D) and the aryl-carbonyl bond (steps E and F) is promoted at elevated temperature (473-573 K) with the formation of toluene and benzene. In the conversion of

nitrobenzene (**Fig. 9(II)**) nitro group interaction with oxygen vacancies (steps A and B) has been proposed [72]. Attachment to surface vacancies can also stabilise the nitro group with lower resultant reaction rates but the greater reactivity of the $-\text{NO}_2$ function (relative to $-\text{CH}=\text{O}$) resulted in measurable activity for each catalyst at 413 K. Interaction of $-\text{NO}_2$ with an oxygen vacancy and N–O bond dissociation generates nitrosobenzene (step C) with subsequent reduction to a phenylhydroxylamine intermediate (step D) and aniline formation and release (step E) [68]. Dissociative interaction of H_2O with oxygen vacancies serves to re-oxidise the support.

4. Conclusions

We have demonstrated that oxide support reducibility and Au size (mean = 2-8 nm) governs the catalytic performance of Au in the reduction of $-\text{CH}=\text{O}$ (benzaldehyde) and $-\text{NO}_2$ (nitrobenzene). TPR coupled with oxygen chemisorption has established partial support (TiO_2 , CeO_2 , $\alpha\text{-Fe}_2\text{O}_3$ and Fe_3O_4) reduction due to the action of spillover hydrogen generated by H_2 dissociation on Au. XPS analysis provided evidence of electron transfer between Au and the oxide carriers. Increasing reaction rates were observed with decreasing Au size (from 8 to 4 nm) with measurably lower rates over Au <3 nm. Gold on reducible supports (CeO_2 , $\alpha\text{-Fe}_2\text{O}_3$ and Fe_3O_4 where $E_{\text{redox}} > 0$) exhibited lower benzaldehyde and nitrobenzene *TOF* relative to $\text{Au}/\gamma\text{-Al}_2\text{O}_3$, Au/TiO_2 and Au/ZrO_2 ($E_{\text{redox}} < 0$), which we attribute to inhibition due to the action of surface oxygen vacancies. There was no measurable benzaldehyde hydrogenation activity over Au/CeO_2 , $\text{Au}/\alpha\text{-Fe}_2\text{O}_3$ and $\text{Au}/\text{Fe}_3\text{O}_4$ at 413 K. Reaction at higher temperatures generated toluene as principal product with secondary benzene formation and no detectable alcohol production. In contrast, reaction over $\text{Au}/\gamma\text{-Al}_2\text{O}_3$ resulted in exclusive benzyl alcohol formation at 413 K with a progressive shift to hydrogenolysis (to toluene and benzene) at higher temperatures.

Acknowledgements

The authors are grateful to Dr. N. Perret for her involvement in this work. EPSRC support for free access to the TEM facility at the University of St. Andrews and financial support to M. Li and X. Wang through the Overseas Research Students Award Scheme (ORSAS) are also acknowledged.

References

- [1] M. Turáková, T. Salmi, K. Eränen, J. Wärnå, D. Y. Murzin, M. Králik, *Appl. Catal. A: Gen.* 499 (2015) 66-76.
- [2] J. Scognamiglio, L. Jones, D. Vitale, C. S. Letizia, A. M. Api, *Food Chem. Toxicol.* 50, Supplement 2 (2012) S140-S160.
- [3] V. van Brunt, J. S. Kanel, in: S. Kulprathipanja (Ed.), *Reactive Separation Processes*, Taylor & Francis, London, 2002, pp. 51-92.
- [4] R. J. Giraud, P. A. Williams, A. Sehgal, E. Ponnusamy, A. K. Phillips, J. B. Manley, *ACS Sust. Chem. Eng.* 2 (2014) 2237-2242.
- [5] T. Mitsudome, K. Kaneda, *Green Chem.* 15 (2013) 2636-2654.
- [6] E. Bus, J. T. Miller, J. A. van Bokhoven, *J. Phys. Chem. B* 109 (2005) 14581-14587.
- [7] L. McEwan, M. Julius, S. Roberts, J. C. Q. Fletcher, *Gold Bull.* 43 (2010) 298-306.
- [8] M. Pan, A. J. Brush, Z. D. Pozun, H. C. Ham, W.-Y. Yu, G. Henkelman, G. S. Hwang, C. B. Mullins, *Chem. Soc. Rev.* 42 (2013) 5002-5013.
- [9] A. Corma, P. Serna, H. García, *J. Am. Chem. Soc.* 129 (2007) 6358-6359.
- [10] A. Taketoshi, M. Haruta, *Chem. Lett.* 43 (2014) 380-387.
- [11] M. Okumura, T. Akita, M. Haruta, *Catal. Today* 74 (2002) 265-269.
- [12] X. Wang, N. Perret, M. A. Keane, *Appl. Catal. A: Gen.* 467 (2013) 575-584.
- [13] R. Zanella, C. Louis, S. Giorgio, R. Touroude, *J. Catal.* 223 (2004) 328-339.
- [14] U. Hartfelder, C. Kartusch, M. Makosch, M. Rovezzi, J. Sa, J. A. van Bokhoven, *Catal. Sci. Technol.* 3 (2013) 454-461.
- [15] C. Milone, R. Ingoglia, L. Schipilliti, C. Crisafulli, G. Neri, S. Galvagno, *J. Catal.* 236 (2005) 80-90.
- [16] H. Rojas, G. Díaz, J. J. Martínez, C. Castañeda, A. Gómez-Cortés, J. Arenas-Alatorre, *J. Mol. Catal. A: Chem.* 363-364 (2012) 122-128.
- [17] M. Boronat, P. Concepción, A. Corma, S. González, F. Illas, P. Serna, *J. Am. Chem. Soc.* 129 (2007) 16230-16237.
- [18] K. Shimizu, Y. Miyamoto, T. Kawasaki, T. Tanji, Y. Tai, A. Satsuma, *J. Phys. Chem. C* 113 (2009) 17803-17810.
- [19] X. Wang, N. Perret, J. J. Delgado, G. Blanco, X. Chen, C. M. Olmos, S. Bernal, M. A. Keane, *J. Phys. Chem. C* 117 (2013) 994-1005.

- [20] F. Cárdenas-Lizana, S. Gómez-Quero, L. Kiwi-Minsker, M. A. Keane, *Int. J. Nanotech.* 9 (2012) 92-112.
- [21] N. Perret, F. Cárdenas-Lizana, D. Lamey, V. Laporte, L. Kiwi-Minsker, M. A. Keane, *Top. Catal.* 55 (2012) 955-968.
- [22] G. C. Bond, *Molecules* 17 (2012) 1716-1743.
- [23] M. Li, X. Wang, N. Perret, M. A. Keane, *Catal. Commun.* 46 (2014) 187-191.
- [24] J. Lenz, B. C. Campo, M. Alvarez, M. A. Volpe, *J. Catal.* 267 (2009) 50-56.
- [25] X. Zhang, H. Shi, B.-Q. Xu, *J. Catal.* 279 (2011) 75-87.
- [26] G. Jacobs, T. K. Das, Y. Zhang, J. Li, G. Racoillet, B. H. Davis, *Appl. Catal. A: Gen.* 233 (2002) 263-281.
- [27] B. Campo, C. Petit, M. A. Volpe, *J. Catal.* 254 (2008) 71-78.
- [28] L. Delannoy, N. Weiher, N. Tsapatsaris, A. M. Beesley, L. Nchari, S. L.M. Schroeder, C. Louis, *Top. Catal.* 44 (2007) 263-273.
- [29] M. Ousmane, L. F. Liotta, D. di Carlo, G. Pantaleo, A. M. Venezia, G. Deganello, L. Retailleau, A. Boreave, A. Giroir-Fendler, *Appl. Catal. B: Environ.* 101 (2011) 629-637.
- [30] F. Arena, P. Famulari, G. Trunfio, G. Bonura, F. Frusteri, L. Spadaro, *Appl. Catal. B: Environ.* 66 (2006) 81-91.
- [31] D. Andreeva, V. Idakiev, T. Tabakova, L. Ilievaa, P. Falaras, A. Bourlinos, A. Travlos, *Catal. Today* 72 (2002) 51-57.
- [32] G. Jacobs, S. Ricote, P. M. Patterson, U. M. Graham, A. Dozier, S. Khalid, E. Rhodus, B. H. Davis, *Appl. Catal. A: Gen.* 292 (2005) 229-243.
- [33] S. Scirè, C. Crisafulli, S. Minicò, G. G. Condorelli, A. Di Mauro, *J. Mol. Catal. A: Chem.* 284 (2008) 24-32.
- [34] R. Prins, *Chem. Rev.* 112 (2012) 2714-2738.
- [35] C. Amorim, M. A. Keane, *J. Hazard. Mater.* 211-212 (2012) 208-217.
- [36] K.-D. Jung, A. T. Bell, *J. Catal.* 193 (2000) 207-223.
- [37] H. Ishikawa, J. N. Kondo, K. Domen, *J. Phys. Chem. B* 103 (1999) 3229-3234.
- [38] D. Haffad, U. Kameswari, M. M. Bettahar, A. Chambellan, J. C. Lavalley, *J. Catal.* 172 (1997) 85-92.
- [39] M. V. Ganduglia-Pirovano, A. Hofmann, J. Sauer, *Surf. Sci. Rep.* 62 (2007) 219-270.
- [40] F. Boccuzzi, A. Chiorino, M. Manzoli, D. Andreeva, T. Tabakova, *J. Catal.* 188 (1999) 176-185.
- [41] T. Tabakova, F. Boccuzzi, M. Manzoli, D. Andreeva, *Appl. Catal. A: Gen.* 252 (2003) 385-397.
- [42] T. Tabakova, G. Avgouropoulos, J. Papavasiliou, M. Manzoli, F. Boccuzzi, K. Tenchev, F. Vindigni, T. Ioannides, *Appl. Catal. B: Environ.* 101 (2011) 256-265.
- [43] G. C. Bond, C. Louis, D. T. Thompson, *Catalysis by Gold*, Imperial College Press, London,

- 2006.
- [44] G. L. Haller, D. E. Resasco, *Adv. Catal.* 36 (1989) 173-235.
- [45] C. Mohr, H. Hofmeister, P. Claus, *J. Catal.* 213 (2003) 86-94.
- [46] L. F. Liotta, G. Pantaleo, F. Puleo, A. M. Venezia, *Catal. Today* 187 (2012) 10-19.
- [47] N. Perret, X. Wang, L. Delannoy, C. Potvin, C. Louis, M. A. Keane, *J. Catal.* 286 (2012) 172-183.
- [48] F. Moreau, G. C. Bond, A. O. Taylor, *J. Catal.* 231 (2005) 105-114.
- [49] S. Arrii, F. Morfin, A. J. Renouprez, J. L. Rousset, *J. Am. Chem. Soc.* 126 (2004) 1199-1205.
- [50] S. Schimpf, M. Lucas, C. Mohr, U. Rodemerck, A. Brückner, J. Radnick, H. Hofmeister, P. Claus, *Catal. Today* 72 (2002) 63-78.
- [51] A. M. Visco, F. Neri, G. Neri, A. Donato, C. Milone, S. Galvagno, *Phys. Chem. Chem. Phys.* 1 (1999) 2869-2873.
- [52] Y.-F. Han, Z. Zhong, K. Ramesh, F. Chen, L. Chen, T. White, Q. Tay, S. N. Yaakub, Z. Wang, *J. Phys. Chem. C* 111 (2007) 8410-8413.
- [53] W. Deng, A. I. Frenkel, R. Si, M. Flytzani-Stephanopoulos, *J. Phys. Chem. C* 112 (2008) 12834-12840.
- [54] A. N. Pestryakov, V. V. Lunin, A. N. Kharlanov, D. I. Kochubey, N. Bogdanchikova, A. Yu. Stakheev, *J. Mol. Struct.* 642 (2002) 129-136.
- [55] S. Peters, S. Peredkov, M. Neeb, W. Eberhardt, M. Al-Hada, *Surf. Sci.* 608 (2013) 129-134.
- [56] A. Saadi, Z. Rassoul, M. M. Bettahar, *J. Mol. Catal. A: Chem.* 164 (2000) 205-216.
- [57] A. Saadi, R. Merabti, Z. Rassoul, M. M. Bettahar, *J. Mol. Catal. A: Chem.* 253 (2006) 79-85.
- [58] M. Chen, D. W. Goodman, *Acc. Chem. Res.* 39 (2006) 739-746.
- [59] P. Claus, A. Brückner, C. Mohr, H. Hofmeister, *J. Am. Chem. Soc.* 122 (2000) 11430-11439.
- [60] M. Arai, A. Obata, Y. Nishiyama, *React. Kinet. Catal. Lett.* 61 (1997) 275-280.
- [61] C. T. Campbell, C. H. F. Peden, *Science* 309 (2005) 713-714.
- [62] C. Milone, C. Crisafulli, R. Ingoglia, L. Schipilliti, S. Galvagno, *Catal. Today* 122 (2007) 341-351.
- [63] M. A. Keane, *J. Mol. Catal. A: Chem.* 118 (1997) 261-269.
- [64] M. A. Vannice, D. Poondi, *J. Catal.* 169 (1997) 166-175.
- [65] H. He, H. X. Dai, L. H. Ng, K. W. Wong, C. T. Au, *J. Catal.* 206 (2002) 1-13.
- [66] J. A. Rodriguez, S. Ma, P. Liu, J. Hrbek, J. Evans, M. Pérez, *Science* 318 (2007) 1757-1760.
- [67] T.-J. Huang, H.-J. Lin, T.-C. Yu, *Catal. Lett.* 105 (2005) 239-247.
- [68] C. Doornkamp, V. Ponec, *J. Mol. Catal. A: Chem.* 162 (2000) 19-32.
- [69] A. Sepúlveda-Escribano, F. Coloma, F. Rodríguez-Reinoso, *J. Catal.* 178 (1998) 649-657.
- [70] S. Sitthisa, T. Sooknoi, Y. Ma, P. B. Balbuena, D. E. Resasco, *J. Catal.* 277 (2011) 1-13.
- [71] N. Perret, X. Wang, T. Onfroy, C. Calers, M. A. Keane, *J. Catal.* 309 (2014) 333-342.
- [72] A. Maltha, S. C. van Wermeskerken, T. L. F. Favre, P. Angevaere, E. J. Grootendorst, C. A.

Koutstaal, A. P. Zuur, V. Ponec, *Catal. Today* 10 (1991) 387-391.

Table 1: Gold loading, specific surface area (SSA), pore volume, Au particle size from TEM/STEM analysis (d), H₂ consumption during temperature programmed reduction (TPR) and requirements for reduction of the Au precursor, H₂ and O₂ chemisorption (post-TPR), H₂ released during temperature programmed desorption (TPD), support point of zero charge (pH_{pzc}), Au 4f_{7/2} binding energy (BE) and standard redox potential (E_{redox}) of the supports.

Catalyst	Au loading (% w/w)	SSA (m ² g ⁻¹)	Pore volume (cm ³ g ⁻¹)	d (nm)	TPR H ₂ consumption (μmol g ⁻¹)	H ₂ chemisorption (μmol g _{Au} ⁻¹)	H ₂ desorbed (mmol g _{Au} ⁻¹)	O ₂ chemisorption (μmol g ⁻¹)	pH _{pzc} ^c	Au 4f _{7/2} BE (eV)	E_{redox} (V)
Au/γ-Al ₂ O ₃	1.1	166	0.36	4.3	87 ^a /84 ^b	318	51	1	7.1	83.3	-1.7
Au/TiO ₂	1.3	44	0.12	4.5	126 ^a /91 ^b	162	9	5	6.7	83.5	-0.6
Au/ZrO ₂	1.0	93	0.13	7.0	56 ^a /61 ^b	137	28	3	7.4	83.6	-1.5
Au/CeO ₂	3.0	108	0.15	2.0	553 ^a /231 ^b	58	6	132	6.8	84.7	1.6
Au/α-Fe ₂ O ₃	1.2	57	0.16	2.6	750 ^a /93 ^b	72	4	168	8.1	84.2	0.8
Au/Fe ₃ O ₄	0.9	11	0.02	7.6	500 ^a /90 ^b	<1	<1	58	5.8	84.1	0.1

^aexperimental value obtained from TPR analysis

^bcalculated value for Au³⁺ → Au⁰

Table 2: Effect of reaction temperature on turnover frequency (*TOF*) and product selectivity (S_j) for the conversion of benzaldehyde over Au/ γ -Al₂O₃, Au/Fe₃O₄ and Au/CeO₂.

Catalyst	<i>T</i> (K)	<i>TOF</i> (h ⁻¹)	S_{benzene} (%)	S_{toluene} (%)	$S_{\text{benzyl alcohol}}$ (%)
Au/ γ -Al ₂ O ₃	413	82	0	0	100
	473	126	0	70	30
	573	258	71	21	8
Au/Fe ₃ O ₄	413	^a	-	-	-
	473	192	10	90	0
	573	378	21	79	0
Au/CeO ₂	413	^a	-	-	-
	473	8	0	100	0
	573	49	20	80	0

^ano detectable activity

Table 3: Benzyl alcohol turnover frequency (*TOF*) and product selectivity (S_j) for reaction over Au/Fe₃O₄ and Au/CeO₂: $T = 573$ K.

Catalyst	<i>TOF</i> (h ⁻¹)	S_{benzene} (%)	S_{toluene} (%)	$S_{\text{benzaldehyde}}$ (%)
Au/Fe ₃ O ₄	364	0	95	5
Au/CeO ₂	17	8	17	75

Figure captions

Fig. 1: Temperature programmed reduction (TPR) profiles for **(I)** supported Au (solid lines) and **(II)** the corresponding supports (dotted lines): **(A)** γ -Al₂O₃, **(B)** TiO₂, **(C)** ZrO₂, **(D)** CeO₂, **(E)** α -Fe₂O₃, **(F)** Fe₃O₄.

Fig. 2: Hydrogen temperature programmed desorption (TPD) profiles: **(A)** Au/ γ -Al₂O₃, **(B)** Au/TiO₂, **(C)** Au/ZrO₂, **(D)** Au/CeO₂, **(E)** Au/ α -Fe₂O₃, **(F)** Au/Fe₃O₄.

Fig. 3: XRD patterns for activated/passivated **(A)** Au/ γ -Al₂O₃, **(B)** Au/TiO₂, **(C)** Au/ZrO₂, **(D)** Au/CeO₂, **(E)** Au/ α -Fe₂O₃ and **(F)** Au/Fe₃O₄; reference JCPDS-ICDD patterns (see card No. in **section 2.2**) are included for Au, γ -Al₂O₃, anatase TiO₂ (A-TiO₂), rutile TiO₂ (R-TiO₂), monoclinic ZrO₂ (M-ZrO₂), tetragonal ZrO₂ (T-ZrO₂), CeO₂, α -Fe₂O₃ (hematite) and Fe₃O₄ (magnetite).

Fig. 4: Representative TEM/STEM images of **(A)** Au/ γ -Al₂O₃, **(B)** Au/TiO₂, **(C)** Au/ZrO₂, **(D)** Au/CeO₂, **(E)** Au/ α -Fe₂O₃ and **(F)** Au/Fe₃O₄ with associated Au size distribution histograms.

Fig. 5: XPS spectra over the Au 4f region for **(A)** Au/ γ -Al₂O₃, **(B)** Au/TiO₂, **(C)** Au/ZrO₂, **(D)** Au/CeO₂, **(E)** Au/ α -Fe₂O₃ and **(F)** Au/Fe₃O₄; experimental data are given by ■ where lines represent data fitting with peak deconvolution.

Fig. 6: Dependence of Au 4f_{7/2} binding energy (BE) on the standard redox potential (E_{redox}) of the oxide supports: **(A)** ◆ Au/ γ -Al₂O₃; **(B)** ◀ Au/TiO₂; **(C)** ▶ Au/ZrO₂; **(D)** ▲ Au/CeO₂; **(E)** ▼ Au/ α -Fe₂O₃; **(F)** ■ Au/Fe₃O₄.

Fig. 7: **(I)** Benzaldehyde ($T = 413$ K, $n/F = 1.2 \times 10^{-3}$ h) and **(II)** nitrobenzene ($T = 413$ K, $n/F = 3.7 \times 10^{-3}$ h) turnover frequency (TOF) as a function of Au particle size (d): **(A)** ◆ Au/ γ -Al₂O₃; **(B)** ◀ Au/TiO₂; **(C)** ▶ Au/ZrO₂; **(D)** ▲ Au/CeO₂; **(E)** ▼ Au/ α -Fe₂O₃; **(F)** ■ Au/Fe₃O₄.

Fig. 8: Dependence of turnover frequency (*TOF*) on the standard redox potential of the oxide supports (E_{redox} from [38]) in **(I)** benzaldehyde and **(II)** nitrobenzene hydrogenation: **(A)** ◆ Au/ γ -Al₂O₃; **(B)** ◀ Au/TiO₂; **(C)** ▶ Au/ZrO₂; **(D)** ▲ Au/CeO₂; **(E)** ▼ Au/ α -Fe₂O₃; **(F)** ■ Au/Fe₃O₄.

Fig. 9: Proposed reaction mechanism for **(I)** benzaldehyde and **(II)** nitrobenzene hydrogenation over Au on reducible supports; M = Ce or Fe.

Fig. 10: Proposed reaction mechanism for benzaldehyde hydrogenation over Au/ γ -Al₂O₃ (M = Al) at different reaction temperatures.

Fig. 1

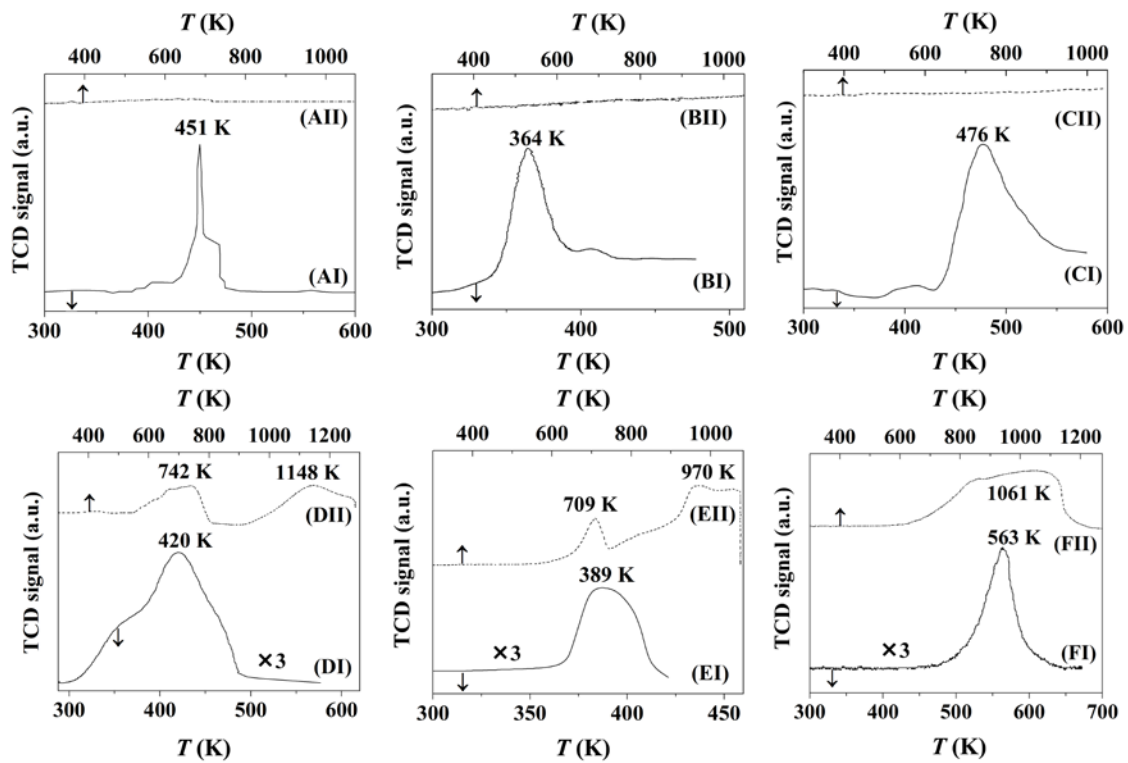


Fig. 2

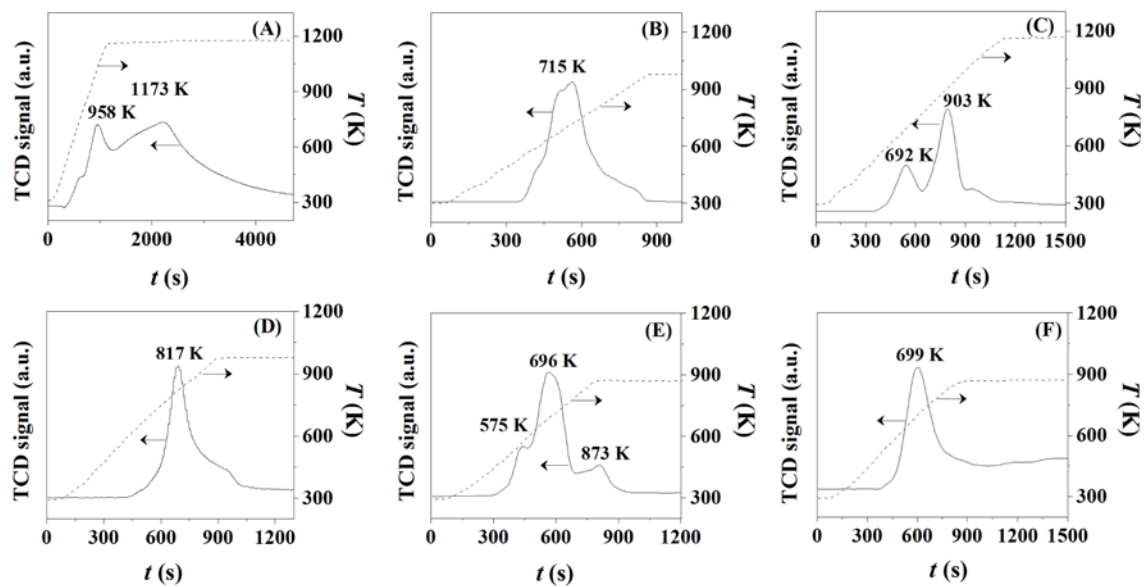


Fig. 3

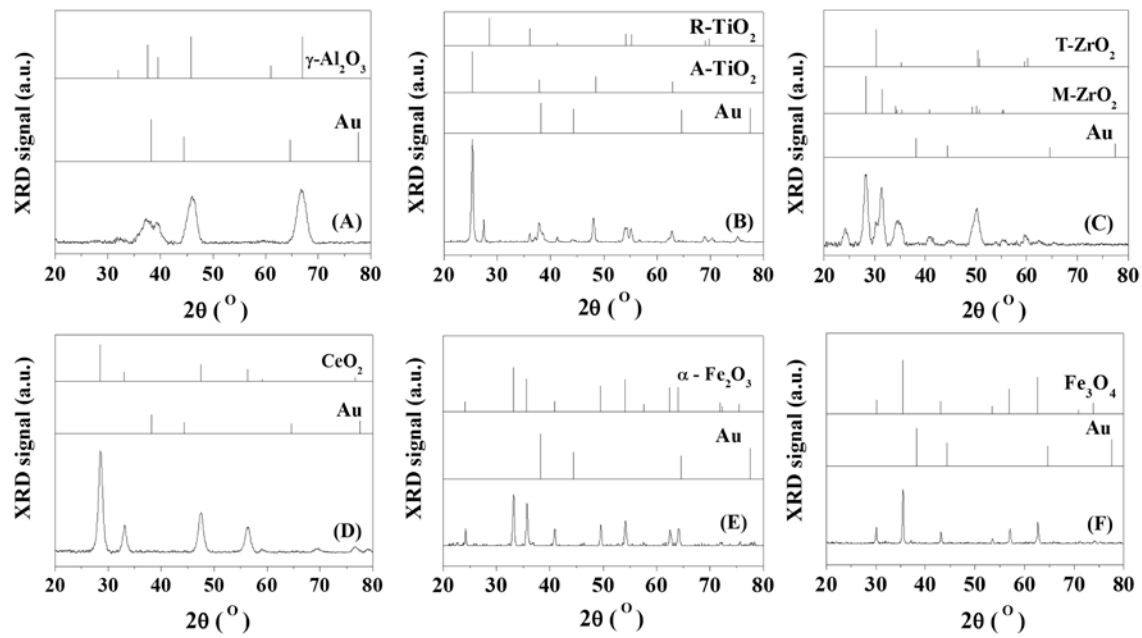


Fig. 4

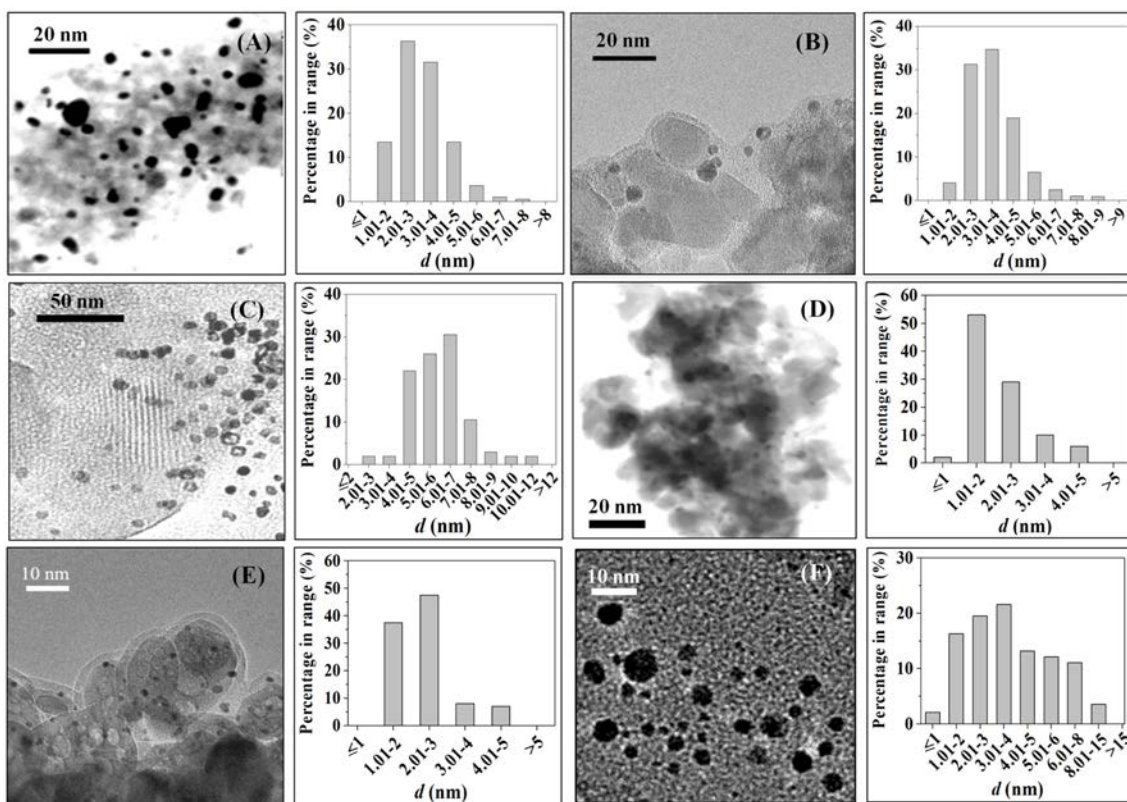


Fig. 5

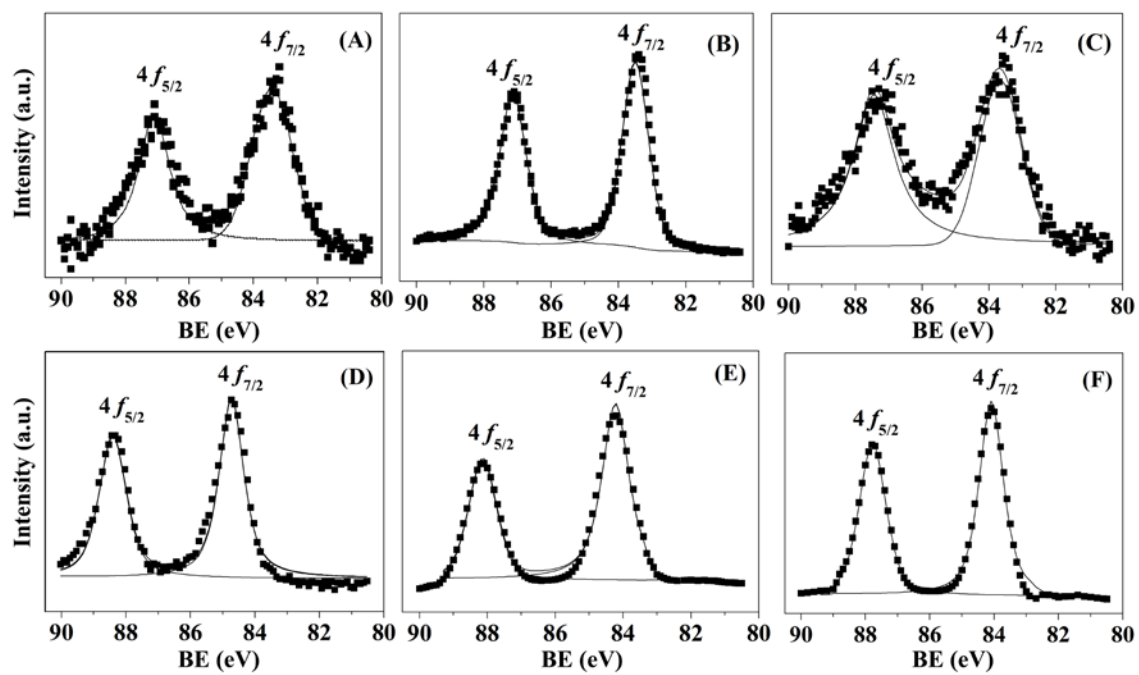


Fig. 6

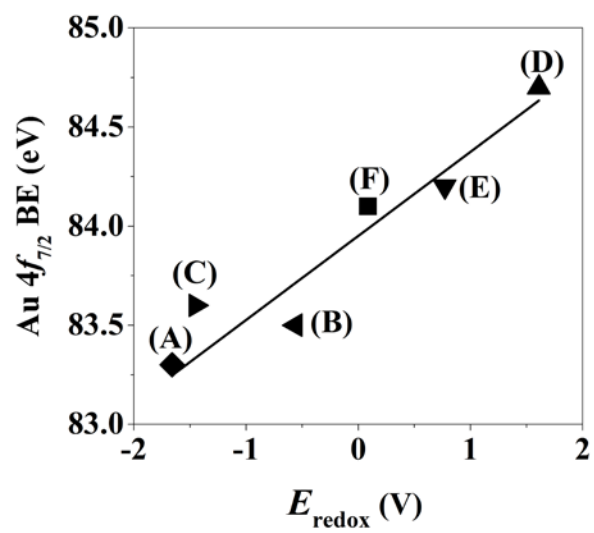


Fig. 7

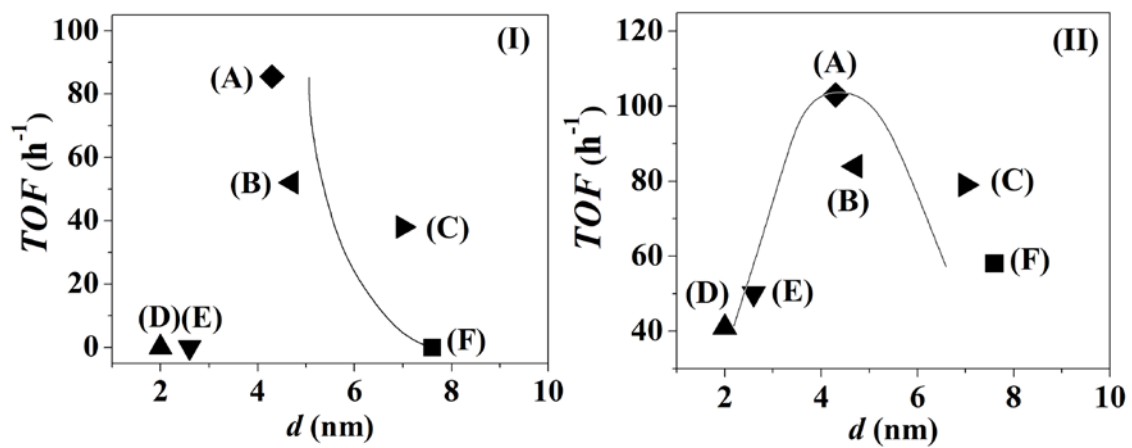


Fig. 8

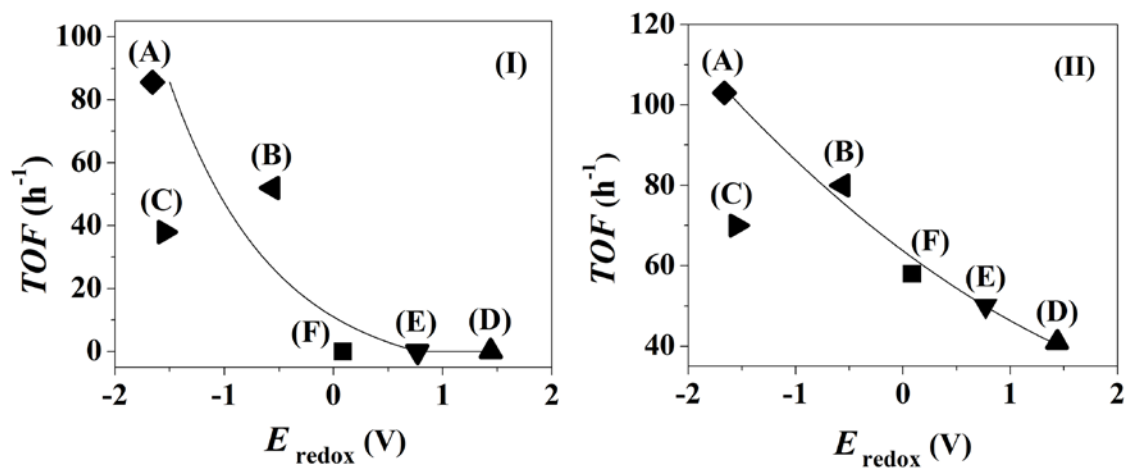


Fig. 9

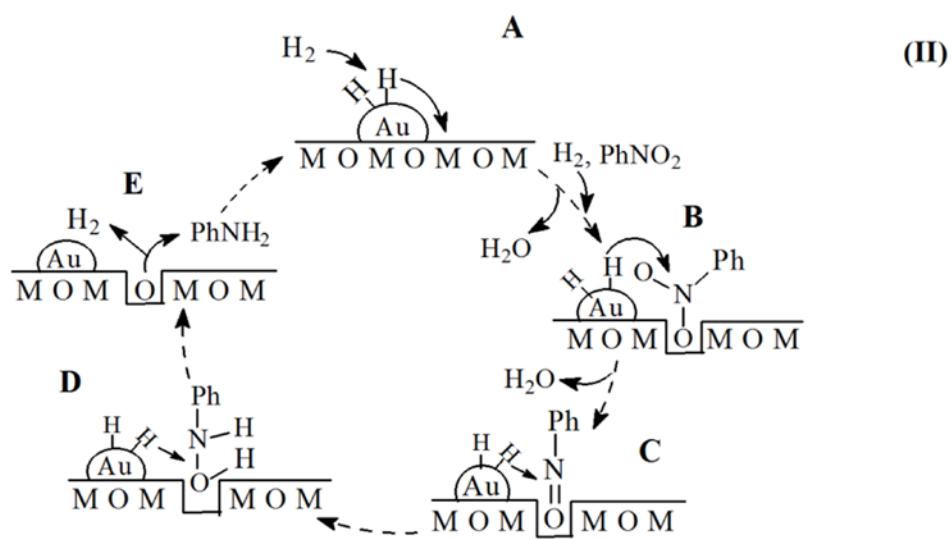
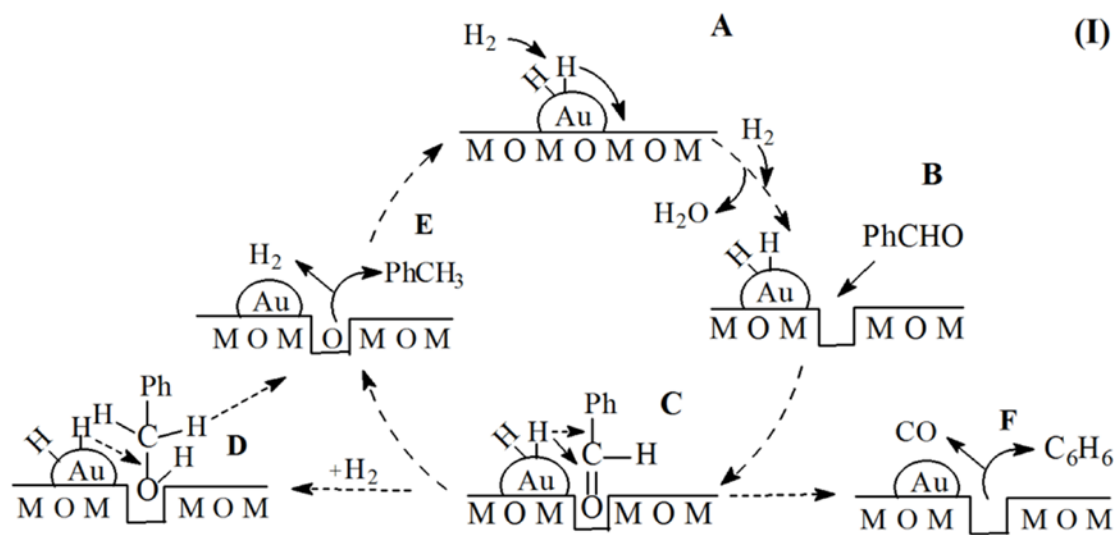


Fig. 10

